waves that propagate from the lower atmosphere and modified by the in situ heating caused by the absorption of near-IR radiation by CO_2. These processes are of key importance for our understanding of the upper atmosphere dynamics (and thus for future aeroassistance manoeuver, for instance), but they remain poorly understood: Numerical simulations results are model-dependent (*25*), and few observations are available. Within this context, the NO emission process identified here provides a powerful way to constrain GCM model behavior above 60 km in conjunction with spacecraft drag measurements (*26*). In particular, the GCM (*25*) predicts that, during the opposite season, the Hadley circulation globally extends to the polar regions because of the stronger solar forcing near perihelion and a dustier atmosphere. This circulation creates a downward flow above the high northern latitudes in the polar night, which is predicted to be about several times stronger than that during the southern winter. We should expect accordingly a much more intense NO emission in July and August 2005.

References and Notes

1. J. L. Fox, in *Venus and Mars: Atmospheres, Ionospheres, and Solar Wind Interactions*, J. Luhmann et al., Eds. [*Geophys. Monogr. Am. Geophys. Union 66* (1992)], pp. 191–222.
2. C. A. Barth *et al.*, *J. Geophys. Res.* **76**, 2213 (1971).
3. C. A. Barth *et al.*, in *Mars*, H. Kieffer *et al.*, Eds. (University of Arizona Press, Tucson, AZ, 1992), pp. 1054–1089, and references therein.
4. J. L. Bertaux *et al.*, *Planet. Space Sci.* **48**, 1303 (2000).
5. J. L. Bertaux *et al.*, *Adv. Space Res.*, in press.
6. J. L. Bertaux *et al.*, in *Mars Express*, A. Chicarro. Ed. (European Space Agency Special Publication SP1240, ESTEC, Netherlands, 2004), pp. 95–120.
7. The instantaneous field of view for bands 0 and 1 (narrow slit) is 0.02° by 0.32° parallel to the limb and 0.2° by 0.32° for bands 2 to 4 (wide slit). Projected at the limb distance of 1200 km, it corresponds to 0.4 km by 6.7 km and 4 km by 6.7 km, respectively, for the narrow and wide slit bands.
8. C. A. Barth, J. B. Pearce, K. K. Kelly, L. Wallace, W. G. Fastie, *Science* **158**, 1675 (1967).
9. A. I. Stewart, D. E. Anderson Jr., L. W. Esposito, C. A. Barth, *Science* **203**, 777 (1979).
10. P. D. Feldman, H. W. Moos, J. T. Clarke, A. L. Lane, *Nature* **279**, 221 (1979).
11. A. I. Stewart, C. A. Barth, *Science* **205**, 59 (1979).
12. A. I. Stewart, J. C. Gerard, D. W. Rusch, S. W. Bougher, *J. Geophys. Res.* **85**, 7861 (1980).
13. S. W. Bougher, J. C. Gerard, A. I. F. Stewart, C. G. Fesen, *J. Geophys. Res.* **95**, 6271 (1990).
14. S. W. Bougher, M. J. Alexander, H. G. Mayr, in *Venus II*, S. W. Bougher, D. M. Hunten, R. J. Phillips, Eds. (University of Arizona Press, Tucson, AZ, 1997), pp. 259–291.
15. The CO_2 cross section at Lα (121.5 nm) is 6.11×10^{-20} cm^{-2}. Optical thickness unity ($\tau = 1$, attenuation factor e) may be determined from the Lα light curve occurring at an altitude of 102 ± 2 km and corresponding to 1.64×10^{19} cm^{-2} CO_2 slant density (local CO_2 density integrated along a line of sight). This shows how Lα emission observations on the night side can be used to determine the density profile around 100 km (and temperature from scale height).
16. These results agree with our night star occultation measurements (*27*).
17. The CO_2 cross section is 3.0×10^{-23} cm^2 at 190 nm, the shortest wavelength of the observed NO band, and decreases very fast with increasing wavelength, and the slant CO_2 density $1/\sigma = 3.3\ 10^{22}$ cm^{-2} is obtained, according to stellar occultations measurements, around 53 km. Therefore, to first order we consider that the CO_2 atmosphere is transparent to the NO emission band above 40 to 50 km. The decrease of emission with decreasing altitude is therefore more a "shell" effect than absorption or extinction by CO_2.
18. J. C. Gerard, A. I. F. Stewart, S. W. Bougher, *Geophys. Res. Lett.* **8**, 633 (1981).
19. A. E. Hedin, H. B. Niemann, W. T. Kasprzak, A. Seiff, *J. Geophys. Res.* **88**, 73 (1983).
20. Assuming a spherical shell between 60 and 80 km with a constant NO δ band emissivity as suggested by Fig. 4, the ratio of horizontal to vertical intensity is 26.
21. J. C. Gérard, E. J. Deneye, H. Lehro, *Icarus* **75**, 171 (1988).
22. R. P. McCoy, *J. Geophys. Res.* **88**, 3197 (1983).
23. The equator of Mars is inclined by 24° to the ecliptic plane. Seasons on Mars are defined by the solar longitude L_s, with $L_s = 0°$ at the northern spring equinox and $L_s = 90°$ at northern summer. Seasons are asymmetric between north and south, because Mars is much nearer to the Sun during southern summer (1.38 AU) than during northern summer (1.66 AU).
24. A similar diabatic subsidence of the atmosphere is also observed on Earth above the winter pole, compensated by a horizontal flow at the mesopause altitude (85 km). In view of the similarities of the atmosphere of Mars with the Earth's stratosphere, this is likely to happen also on Mars, and the CO_2 condensation process on the winter pole on Mars can only emphasize this subsidence on Mars.
25. F. Forget *et al.*, *J. Geophys. Res.* **104**, 24155 (1999).
26. G. M. Keating, M. Theriot, R. Tolson, in proceedings of *Mars Atmosphere Modelling and Observations Workshop*, Grenada, Spain, CNES/ESA, 13 to 15 January 2003.
27. X. Quemerais *et al.*, in preparation.
28. Mars Express is a space mission from European Space Agency (ESA). We wish to express our gratitude to all ESA members who participated in this successful mission, in particular M. Denis at European Space Operations Center for the delicate controlling of the spacecraft and R. Pischel and T. Zeghers at ESTEC for careful planning exercises and supporting geometry graphics. We thank also Astrium for the design and construction of the spacecraft, in particular A. Clochet, responsible for the payload; our collaborators at the three institutes for the design and fabrication of the instrument (Service d'Aéronomie, France; BIRA, Belgium; and IKI, Moscow); and CNRS and CNES for financing SPICAM in France, the Belgian government, the Russian Academy of Sciences, and NASA, for support of U.S. co-investigators. The SPICAM team is composed of the following members: J.-L. Bertaux[1] (principal investigator), O. Korablev,[2] D. Fonteyn,[3] E. Chassefière,[1] E. Dimarellis,[1] J. P. Dubois,[1] A. Hauchecorne,[1] F. Lefèvre, A. C. Levasseur-Regourd,[1] G. Cernogora,[1] M. Cabane,[1] P. Rannou,[1] E. Quémerais,[1] C. Hermans,[1] G. Kockarts,[1] C. Lippens,[1] M. De Maziere,[1] D. Moreau,[1] C. Muller,[1] E. Neefs,[1] D. Nevejans, P. C. Simon,[1] F. Forget,[4] F. Hourdin,[4] O. Talagrand,[4] V. I. Moroz,[2] A. Rodin,[2] B. Sandel,[5] A. Stern,[6] F. Leblanc,[1] F.Montmessin,[1,7] O. Witasse,[8] B. Gondet,[9] A. Federova,[2] D. Fussen,[3] E. Kyrola,[10] J. Tamminen,[10] S. Lebonnois,[4] S. Perrier.[1]

[1]Service d'Aéronomie du CNRS/IPSL, BP.3, 91371, Verrières-le-Buisson, France. [2]IKI, 84/32 Profsoyuznaya, 117810 Moscow, Russia. [3]BIRA, 3 Avenue Circulaire, B-1180 Brussels, Belgium. [4]Laboratoire de Météorologie Dynamique/IPSL, Université Paris 6, 75252 Paris, France. [5]Lunar and Planetary Laboratory, 1541 East University Boulevard, University of Arizona, Tucson, AZ 85721, USA. [6]Southwest Research Institute, Boulder, CO 80302, USA. [7]NASA Ames Research Center, Moffett Field, CA 94035–1000, USA. [8]ESTEC/SCI-SR postbus 299, 2200 AG Noordwijk, Netherlands. [9]Institut d'Astrophysique Spatiale, Orsay Campus, 91405 Orsay, France. [10]Finnish Meteorological Institute, Post Office Box 503, Fin-00101 Helsinki, Finland.

1 November 2004; accepted 27 December 2004
10.1126/science.1106957

Prediction of Hydrogen Flux Through Sulfur-Tolerant Binary Alloy Membranes

Preeti Kamakoti,[1,2] Bryan D. Morreale,[1] Michael V. Ciocco,[1] Bret H. Howard,[1] Richard P. Killmeyer,[1] Anthony V. Cugini,[1] David S. Sholl[2]*

Metal membranes play a vital role in hydrogen purification. Defect-free membranes can exhibit effectively infinite selectivity but must also provide high fluxes, resistance to poisoning, long operational lifetimes, and low cost. Alloying offers one route to improve on membranes based on pure metals such as palladium. We show how ab initio calculations and coarse-grained modeling can accurately predict hydrogen fluxes through binary alloy membranes as functions of alloy composition, temperature, and pressure. Our approach, which requires no experimental input apart from knowledge of bulk crystal structures, is demonstrated for palladium-copper alloys, which show nontrivial behavior due to the existence of face-centered cubic and body-centered cubic crystal structures and have the potential to resist sulfur poisoning. The accuracy of our approach is examined by a comparison with extensive experiments using thick foils at elevated temperatures. Our experiments also demonstrate the ability of these membranes to resist poisoning by hydrogen sulfide.

The purification of hydrogen from gas mixtures is a crucial process in both existing and envisioned uses of hydrogen as a chemical feedstock and fuel (*1*, *2*). Membranes made from thin films of metal such as Pd are a well-known technology for achieving this purification. Metal membranes are also used in membrane reactors that boost reaction efficiency by selectively remov-

ing or adding hydrogen (*3*). Any potential metal membrane must simultaneously satisfy multiple performance objectives, such as delivering high hydrogen flux, showing long-term operability over broad ranges of temperature (T) and pressure (P), and resistance to poisoning and degradation by gas contaminants.

One route to improving on the performance of pure metal membranes is to use metal alloys as membranes (*4*). Binary alloys of Pd with many metals have been examined (*5*–*13*). A small number of studies have examined ternary alloys (*4*), but the large experimental investment required to screen even a small number of membranes poses a substantial barrier to studying such alloys in any systematic manner. This situation could be greatly aided if reliable theoretical methods were available to identify alloy compositions with promising properties or to disqualify materials from further investigation. Here we show that a combination of first-principles density functional theory (DFT) calculations and coarse-grained modeling can be used to complement experimental studies by comparing model predictions with extensive experimental measurements of hydrogen permeation through binary Pd-Cu alloys. These alloys are particularly interesting because they may resist poisoning by H_2S (*8*, *10*, *13*–*15*).

The permeation of hydrogen through metal membranes is a multistep process involving dissociative chemisorption of molecular H_2, the diffusion of atomic H into and through the bulk, and recombinative desorption of H_2 from the downstream surface (*16*). We modeled situations where diffusion through the bulk is the dominant resistance to mass transport; that is, where surface reactions are not rate-limiting. (Surface reactions could in principle be included within our modeling framework, but this is beyond the scope of our current work.) Under this assumption, the H concentration θ_H just inside the surface of a membrane is in equilibrium with the partial pressure of H_2 in the neighboring gas phase P_{H_2}. For dilute H concentrations, $\theta_H = K_S P_{H_2}^{1/2}$, where K_S is the Sievert's constant. The flux of H_2 through a membrane is determined by the concentration drop across the membrane and the diffusivity D of dissolved H. For dilute H concentrations, the diffusivity is well described by the self-diffusivity D_s of isolated H atoms in the metal (*17*). The overall throughput of a membrane is typically characterized by the permeability, which in this case is simply $k = 1/2(K_S D_S)$ (*18*).

The aim of our modeling approach is to characterize membrane permeability in a binary alloy membrane with composition A_xB_{100-x} as a function of temperature, pressure, and alloy composition by predicting K_S and D_S. We assume that the crystal structure and the degree of local ordering within the alloy are known, but we do not use any other information that would require experimental determination. We demonstrate our method for Pd_xCu_{100-x}, where x denotes atomic %. Pd_xCu_{100-x} alloys occur in multiple crystal structures (*19*). A disordered face-centered cubic (fcc) phase occurs for a wide range of alloy compositions, including the region with $x > 47$. For a range of compositions centered at $x = 40$ and $T < 773$ K, an ordered body-centered cubic (bcc) phase exists.

To predict H solubility in Pd_xCu_{100-x} alloys, we consider gaseous H_2 in equilibrium with interstitial atomic H in the metal. Molecular H_2 is treated as an ideal gas, which is an accurate approach for a wide range of pressures at elevated temperatures. Interstitial sites in the alloy are treated as independent three-dimensional harmonic oscillators with classical binding energy for atomic H E_b and vibrational frequencies ν_H. The Sievert's constant is calculated by equating the chemical potentials of the interstitial and gaseous species (*20*, *21*) giving

$$K_S = \exp\left(\beta\left[-\frac{D_E}{2} + \frac{h\nu_{H_2}}{4} - E_b - \frac{3}{2}h\nu_H\right]\right) \frac{1}{\sqrt{\alpha}} \sqrt{1 - \exp(-\beta h\nu_{H_2}/2)} \frac{1}{(1 - e^{-\beta h\nu_H})^3} \quad (1)$$

where

$$\alpha = \left(\frac{2\pi mkT}{h^2}\right)^{3/2} \frac{4\pi^2 I(kT)^2}{h^2} \quad (2)$$

Here, $D_E(\nu_{H_2})$ is the classical dissociation energy (vibrational frequency) of gaseous H_2, I is the molecular moment of inertia, m is the mass of H_2, h is Planck's constant, and $\beta = 1/k_BT$ (k_B is the Boltzmann constant).

We calculated E_b and ν_H for representative interstitial sites using plane wave DFT for fcc Pd_xCu_{100-x} (x = 50, 75, and 100) and

[1]U.S. Department of Energy National Energy Technology Laboratory, Pittsburgh, PA 15236, USA. [2]Department of Chemical Engineering, Carnegie Mellon University, Pittsburgh, PA 15213, USA.

*To whom correspondence should be addressed. E-mail: sholl@andrew.cmu.edu

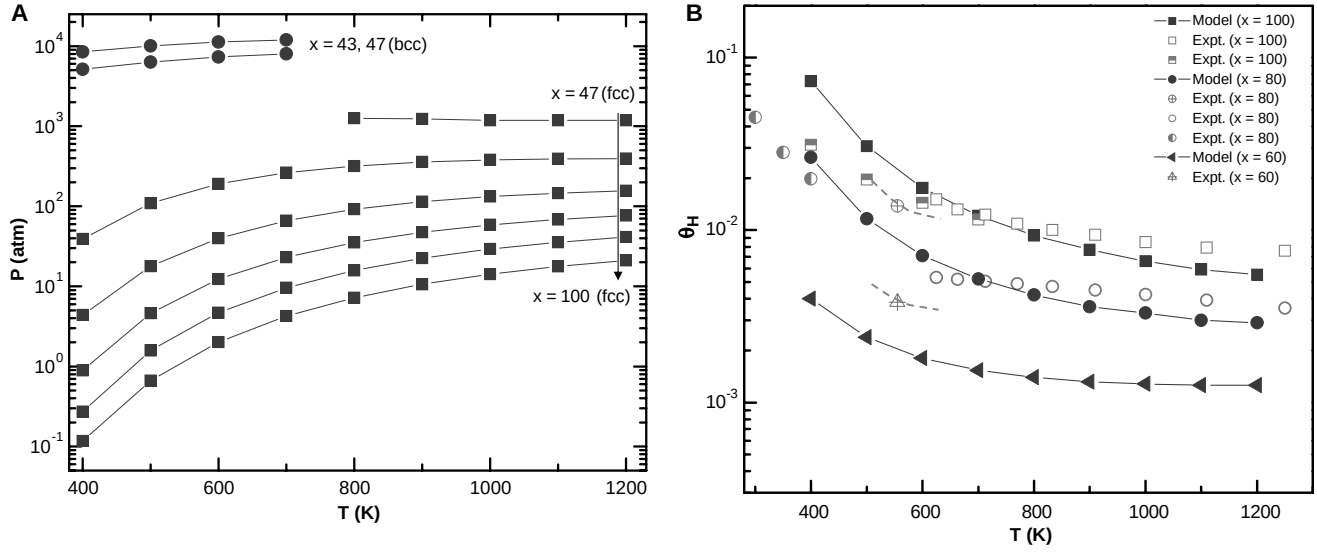

Fig. 1. (**A**) *P-T* diagram showing, for various alloys, the conditions predicted to yield $Pd_xCu_{100-x}H_{2.5}$. Circles correspond to bcc alloys with $x = 43$ (upper curve) and 47 (lower curve). Squares show results for fcc alloys with x = 47, 60, 70, 80, 90, and 100 in descending order. (**B**) Comparison of predicted and experimentally reported hydrogen solubilities in fcc Pd_xCu_{100-x} with $P_{H_2} = 1$ atm for $x = 100$ (squares), 80 (circles), and 60 (triangles). Predictions are indicated by solid curves and solid symbols, whereas experimental data are shown with open symbols. Dashed curves are from the partial molar enthalpy and partial molar excess entropy measured experimentally at 555 K (*31*). The other experimental data are from (*6*, *32*, *33*).

bcc Pd_xCu_{100-x} (x = 35, 43, 47, and 50). Our DFT calculations used the PW91 GGA functional and represented interstitial H at dilute concentrations using a single H atom in computational cells containing 20 to 30 metal atoms (*22*, *23*). Frequencies were estimated via small displacements of the H atom around local minima (or transition states), neglecting coupling of these modes with phonons in the metal (*24*, *25*). In all, we considered 58 distinct octahedral sites and over 100 tetrahedral sites. The results for each crystal structure were used to determine simple expressions correlating the local environment of an interstitial site with the properties of H in that site. For example, for bcc Pd_xCu_{100-x} we find that tetrahedral sites with local composition $Pd_2Cu_2(Pd_2Cu_2)$, $Pd_2Cu_2(PdCu_3)$, $PdCu_3$, and Cu_4 can be assigned binding energies of E_b = 0.03, 0.07, 0.16, and 0.22 eV over the whole range of bcc alloy compositions. The terms in parentheses indicate the composition of the next nearest neighbor shell. We used a more complex expression involving measures of the local and overall alloy composition for the interstitial sites in the fcc alloy (*23*). With E_b defined in this way, the net solubility of a specified alloy is found by applying Eq. 1 to each site.

We report our solubility results by showing in Fig. 1A the *P-T* combinations that are predicted to have 2.5% of interstitial sites filled. The solubility drops drastically as the Pd content of the fcc alloy decreases. For bcc alloys, extremely high pressures are required to obtain even this dilute concentration. For all *P-T* combinations below the curve for an alloy of interest in Fig. 1A, our modeling assumption that H is dilute within a membrane is valid. Our predicted solubilities for hydrogen in fcc Pd_xCu_{100-x} (x = 100, 80, and 60) are compared with experimental data in Fig. 1B. The model predictions are not perfect, but the model does accurately capture the variation in solubility with temperature and, more importantly, with alloy composition. No experimental data are available for comparision for the bcc alloy.

To predict H diffusivities in Pd_xCu_{100-x} alloys, we first extended the DFT-based models described above for the binding energy of interstitial H to a similar description of the transition-state energies that define hops between adjacent sites. These energies, when used in appropriate rate expressions, predict the hopping rates between adjacent sites. We then used kinetic Monte Carlo (KMC) simulations to evaluate the diffusivities of isolated H atoms in systems with large spatial extent. For fcc alloys, quantum-corrected transition-state theory (TST) is used to predict local rates, and transition-state energies for hops between octahedral and tetrahedral sites are predicted using a DFT-based expression that accounts for both the local and overall alloy composition (*23*). The predicted diffusivities for several fcc alloys are shown in Fig. 2. In the range of temperatures relevant to membrane operation, the net activation energy for H diffusion increases, and the net diffusivity decreases as the Cu content of fcc Pd_xCu_{100-x} is increased.

To describe H diffusion in bcc Pd_xCu_{100-x}, we used DFT calculations for materials with x = 35, 43, 47, and 50 and characterized the hopping energies between examples of all possible pairs of adjacent binding sites (characterized as listed above). The classical energy barriers ranged from 0.04 to 0.13 eV and can be reasonably approximated as independent of alloy composition for each type of local hop. Because of the large zero point energies in these materials, quantum-corrected TST for hopping rates between two tetrahedral sites, $k_{T\rightarrow T}$, at elevated temperatures can be simplified to (*26*) $k_{T\rightarrow T} = (k_BT/h)\exp[-\beta E^{qc}]$, where $E^{qc} = E^{classical} + (3/2)h\nu^T - h\nu^{TS}$, where $E^{classical}$ is the classical activation barrier to hopping, and $\nu^T(\nu^{TS})$ is the average vibrational frequency of H in the tetrahedral site (transition state).

Predicted H diffusion coefficients for bcc Pd_xCu_{100-x} are shown in Fig. 2. Consistent with experiments (*27*), the diffusivity is significantly larger than in fcc Pd_xCu_{100-x} alloys and is relatively insensitive to alloy composition. This behavior is consistent with the general observation that H diffusion is more rapid in bcc metals than in fcc metals (*28*). The net activation barrier for diffusion in the bcc alloys is ~0.12 eV. This corresponds to the energy barrier required to achieve long-range diffusion in the ordered alloy, bcc $Pd_{50}Cu_{50}$. Local hops with lower barriers also exist in this material, but these cannot lead to long-range diffusion, a point we addressed incorrectly in earlier work (*22*). Our prediction is in good agreement with experimental measurements in bcc $Pd_{47}Cu_{53}$ at 298 < T < 623 K, which gave an overall activation energy of 0.11 eV (*27*). Our predictions do not agree with lower-temperature experiments that yielded an activation energy of 0.04 eV (*26*). H diffusion in bcc metals is known to yield different activation energies at low and high temperatures

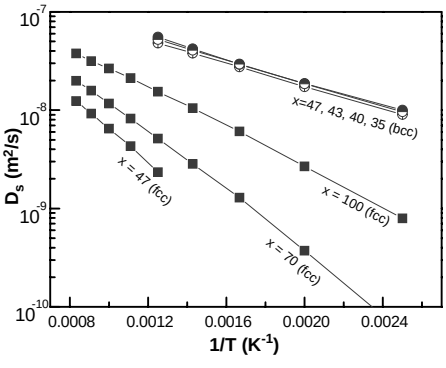

Fig. 2. Predicted diffusion coefficients for interstitial H in fcc Pd_xCu_{100-x} (squares), with x = 100, 70, and 47 in descending order; and bcc Pd_xCu_{100-x} (circles), with x = 47, 43, 40, and 35 in descending order.

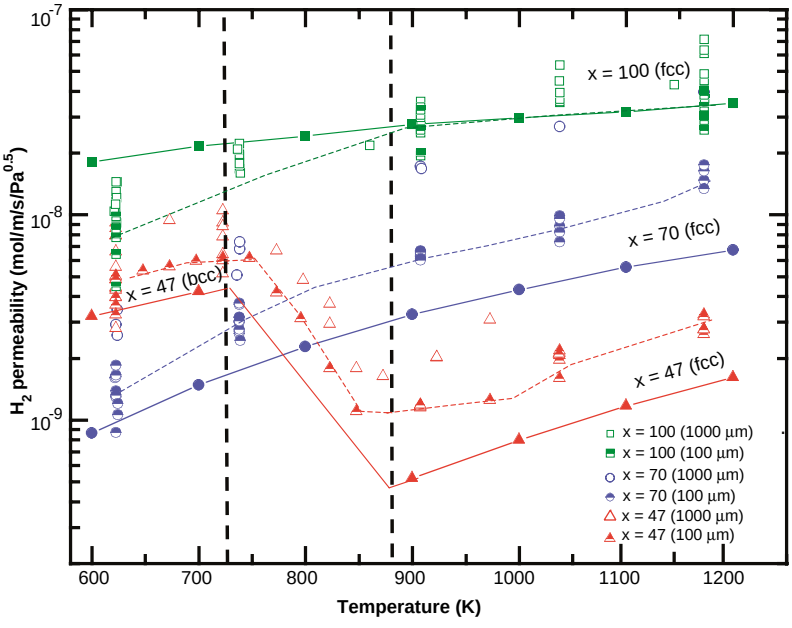

Fig. 3. Predicted and measured H_2 permeabilities through Pd_xCu_{100-x} membranes with x = 100 (squares), x = 70 (circles), and x = 47 (triangles), all in atomic %. The membrane thickness for each set of experiments is indicated in the legend. Theoretical predictions are shown with solid symbols and solid curves. Dashed curves indicate the experimental measurements with a 100-μm membrane (*11*, *18*). All curves are to guide the eye only. The vertical dashed lines indicate the region where the fcc-bcc transition occurs for $Pd_{47}Cu_{53}$ (*10*). Theoretical predictions for this alloy are only shown in the single-phase regions. The theoretical curve indicated in the phase-transition region simply connects the theoretical predictions in the two separate phases.

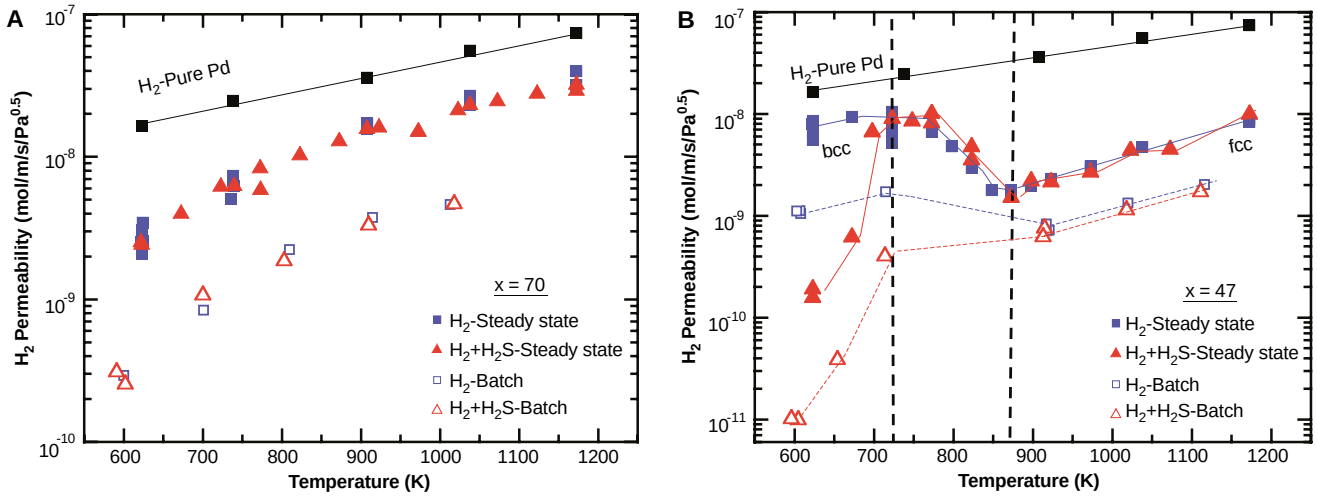

Fig. 4. Experimentally measured permeabilities of Pd_xCu_{100-x} membranes with (**A**) x = 100 and 70 and (**B**) x = 100 and 47. Solid symbols show results from steady-state experiments with 1000-μm foils, whereas the results from transient batch experiments (*10*) with 100-μm foils are shown with open symbols. Experiments performed with pure H_2 and pure Pd are shown as black squares for reference. For PdCu alloys, experiments performed with pure H_2 are shown in blue; experiments performed with H_2 containing 1000 ppm H_2S are shown in red. Curves are to guide the eye only. The vertical dashed lines in (B) indicate the bcc-fcc phase transition region as in Fig. 3.

because of the appearance of quantum effects at low temperatures (*26*). We are primarily interested in describing membranes at temperatures well above room temperature. The model described above is well suited to this regime.

Our DFT-based models of H solubility and diffusion allow us to predict the macroscopic flux of H_2 through alloy membranes. A limited knowledge of the alloy phase diagram was the only experimental information used in deriving these models. The predicted permeabilities for several representative alloys are shown in Fig. 3.

To examine the validity of our predictions, we performed extensive experiments with alloy foils of thickness 100 and 1000 μm with $623 < T < 1173$ K and H_2 pressures ranging from 1 to 26 atm (Fig. 3). Transmembrane fluxes were measured using a steady-state flow system with a pressure drop of 1.36 atm (*11*, *18*). The crystal structure and elemental composition of the foils were verified by x-ray diffraction and inductively coupled plasma analysis, respectively. We observed some variations in permeability as the H_2 pressure and membrane thickness were varied, which may stem from resistances to H transport other than bulk diffusion in the membrane (*18*, *29*). The overall consistency of the data in Fig. 3, however, supports the notion that a description based only on bulk diffusion and solubility is useful for comparing relative permeabilities of different alloys.

Figure 3 compares our model predictions with our experiments for Pd_xCu_{100-x} foils. For pure Pd, the prediction lies within the scatter of the experiments, although the prediction underestimates the true increase in permeability with increasing T. For fcc $Pd_{70}Cu_{30}$, the model predicts the growth rate of permeability with T accurately, although the numerical value is underestimated at all temperatures. $Pd_{47}Cu_{53}$ provides a stringent test of our model, because we observed experimentally (*19*) that this material is in a bcc form for $T < 725$ K and an fcc form for $T > 875$ K. In between these two temperature ranges, a material of mixed crystal structure exists. Our experiments and model predictions both show a dramatic decrease in membrane permeability as T is raised through this phase transition. In both phases, our model accurately predicts the temperature dependence of the permeability while underestimating the absolute values.

Achieving reasonable hydrogen flux is just one of the multiple objectives that must be satisfied by a practical metal membrane; resistance to chemical poisoning and long-term stability are also crucial. Several previous reports have hinted that PdCu alloys might have favorable behaviors in this regard (*8*, *10*, *13*–*15*), so we performed a series of experiments to probe the resistance of our membranes to poisoning by H_2S, a ubiquitous contaminant in many applications. Experiments were performed in a steady-state flow mode, where the feed gas contained 1000 parts per million (ppm) H_2S to complement our previous transient batch experiments (*10*). In the transient experiments, pure H_2 or 1000 ppm H_2S/balance H_2 was charged on the feed side of a membrane to pressures up to 5 atm, and the transient pressure as H_2 permeated through the membrane was monitored (*10*).

The key results of our H_2S tolerance experiments are summarized in Fig. 4. The batch and steady-state experiments yielded consistent results. Essentially no inhibition of H_2 flux was observed for $Pd_{70}Cu_{30}$ membranes (Fig. 4A). We exposed one $Pd_{70}Cu_{30}$ membrane to the flowing 1000 ppm H_2S stream for >175 hours at temperatures ranging from 623 to 1173 K without performance degradation. For $Pd_{47}Cu_{53}$, poisoning of the membrane by H_2S was slight at temperatures where the alloy is an fcc material but stronger at temperatures where the alloy is bcc (Fig. 4B). At $T \sim 600$ K for a H_2 feed containing 1000 ppm H_2S, the permeability of the fcc $Pd_{70}Cu_{30}$ membrane was more than an order of magnitude larger than that of the bcc $Pd_{47}Cu_{53}$ membrane.

The picture that emerges from our modeling and experimental studies of these alloy membranes is entirely consistent. By assuming that diffusion is the rate-limiting step in permeation, our theoretical approach can predictively describe the flux of hydrogen through membranes as a function of alloy composition and temperature. Other elementary steps such as hopping from surface to subsurface sites may play a role in the performance of the ultrathin films that are desirable in practical applications (*8*, *29*, *30*). Extending our first-principles approach to examine these effects will provide useful insights into identifying physical regimes where they might become important. Similarly, identification and detailed modeling of the surface chemistry responsible for the sulfur resistance exhibited by PdCu membranes will likely open the door to the discovery of other alloys with favorable properties as H_2 membranes.

References and Notes

1. Y. S. Lin, *Separ. Purif. Technol.* **25**, 39 (2001).
2. L. Schlapbach, A. Züttel, *Nature* **414**, 353 (2001).
3. Y. She, J. Han, Y. H. Ma, *Catal. Today* **67**, 45 (2001).
4. S. N. Paglieri, J. D. Way, *Sep. Purif. Methods* **31**, 1 (2002).
5. R. B. McLellan, M. Yoshihara, *Acta Metall.* **35**, 197 (1987).
6. A. Weiss, S. Ramaprabhu, N. Rajalakshmi, *Z. Physik Chem.* **199**, 165 (1997).
7. O. M. Lovvik, R. A. Olsen, *J. Alloys Compounds* **330–332**, 332 (2002).

8. F. Roa, J. D. Way, *Ind. Eng. Chem. Res.* **42**, 5827 (2003).
9. F. Roa, J. D. Way, R. L. McCormick, S. Paglieri, *Chem. Eng. J.* **93**, 11 (2003).
10. B. D. Morreale *et al.*, *J. Membr. Sci.* **241**, 219 (2004).
11. B. H. Howard *et al.*, *J. Membr. Sci.* **241**, 207 (2004).
12. V. M. Gryaznov, *Z. Physik Chem.* **147**, 123 (1986).
13. D. L. McKinley, U. S. Patent 3,350,845 (1967).
14. A. Kulprathipanja, G. O. Alptekin, J. L. Falconer, J. D. Way, *Ind. Eng. Chem. Res.* **43**, 4188 (2004).
15. D. Edlund, paper presented at the Advanced Coal-Fired Power Systems '96 Review Meeting, Pittsburgh, PA, 1996.
16. T. L. Ward, T. Dao, *J. Membr. Sci.* **153**, 211 (1999).
17. F. J. Keil, R. Krishna, M. O. Coppens, *Rev. Chem. Eng.* **16**, 71 (2000).
18. B. D. Morreale *et al.*, *J. Membr. Sci.* **212**, 87 (2003).
19. M. Hansen, *Constitution of Binary Alloys* (McGraw-Hill, New York, 1958).
20. R. H. Fowler, C. J. Smithells, *Proc. R. Soc. London Ser. A* **145**, 699 (1937).
21. C. Wagner, *Acta Metallurgica* **21**, 1297 (1973).
22. P. Kamakoti, D. S. Sholl, *J. Membr. Sci.* **225**, 145 (2003).
23. P. Kamakoti, D. S. Sholl, *Phys. Rev. B* **71**, 014301 (2005).
24. J. Greeley, W. P. Krekelberg, M. Mavrikakis, *Angew. Chem. Int. Ed. Engl.* **43**, 4296 (2004).
25. D. E. Jiang, E. A. Carter, *Phys. Rev. B* **70**, 064102 (2004).
26. J. Volkl, G. Alefeld, in *Hydrogen in Metals I*, G. Alefeld, J. Volkl, Eds. (Springer-Verlag, Berlin, 1978), pp. 321–348.
27. J. Piper, *J. App. Phys.* **37**, 715 (1966).
28. Y. Fukai, H. Sugimoto, *Adv. Phys.* **34**, 271 (1985).
29. B. A. McCool, Y. S. Lin, *J. Mat. Sci.* **36**, 3221 (2001).
30. Y. H. Ma *et al.*, *Ind. Eng. Chem. Res.* **43**, 2936 (2004).
31. O. J. Kleppa, Shamsuddin, C. Picard, *J. Chem. Phys.* **71**, 1656 (1979).
32. E. Wicke, H. Brodowsky, in *Hydrogen in Metals 2*, G. Alefeld, J. Volkl, Eds. (Springer-Verlag, Berlin, 1978), pp. 73–151.
33. M. Yoshihara, R. B. McLellan, *Acta Metallurgica* **31**, 66 (1983).
34. Supported by the U.S. Department of Energy's Office of Fossil Energy. B.D.M. and M.V.C. were supported by a Parsons Inc. National Energy Technology Laboratory (NETL) Site Support contract. D.S.S. is an NETL Faculty Fellow.

2 November 2004; accepted 21 December 2004
10.1126/science.1107041

Micropylar Pollen Tube Guidance by Egg Apparatus 1 of Maize

Mihaela L. Márton,[1] Simone Cordts,[1] Jean Broadhvest,[2] Thomas Dresselhaus[1]*

Pollen tube guidance precedes the double fertilization of flowering plants. Here, we report the identification of a small maize protein of 94 amino acids involved in short-range signaling required for pollen tube attraction by the female gametophyte. *ZmEA1* is exclusively expressed in the egg apparatus, consisting of the egg cell and two synergids. Chimeric ZmEA1 fused to green fluorescent protein (ZmEA1:GFP) was first visible within the filiform apparatus and later was localized to nucellar cell walls below the micropylar opening of the ovule. Transgenic down-regulation of the *ZmEA1* gene led to ovule sterility caused by loss of close-range pollen tube guidance to the micropyle.

In contrast to most animal and many lower plant species, sperm cells of flowering plants are nonmotile and are transported from the stigma to the female gametophyte (embryo sac) via pollen tube growth to allow double fertilization (*1*). Genetic and physiological studies have shown the involvement of both female sporophytic and gametophytic tissues in pollen tube guidance of different plant species (*2*). Molecules involved in sporophytic guidance have been identified as γ-aminobutyric acid (GABA), arabinogalactans, and small secreted proteins (*3–6*), but little is known about the molecules produced by the female gametophyte required for pollen tube guidance. The synergids have been identified as the source of producing a short-range pollen tube attractant or attractants in *Torenia fournieri*, but the molecular nature of the attractant(s) is still unknown (*7*).

We report the identification of *ZmEA1* (*Zea mays EGG APPARATUS1*) from an unfertilized maize egg cell cDNA library (*8*) and its role for short-range pollen tube attraction by the female gametophyte. ZmEA1 is produced by the cells of the egg apparatus and represents a highly hydrophobic small protein of 94 amino acids with a predicted transmembrane domain (Fig. 1A). Tissue and single-cell reverse transcription polymerase chain reaction (RT-PCR) analyses showed that *ZmEA1* is exclusively expressed in the maize egg apparatus (Fig. 1, B and C) before fertilization. Lower RNA levels were detected in zygotes after in vitro fertilization and at an even lower level in two-celled proembryos. Expression of *ZmEA1* was no longer detectable at later embryo stages, which suggests a rapid down-regulation of the gene after fertilization. In situ hybridization of the maize ovary (Fig. 2B) and of female gametophyte isolated cells confirmed the restricted expression in the egg apparatus, which lacked detectable signals in the central cell, antipodals, and nucellar and integumental cells. Out of 988 ESTs generated from the originating cDNA library, 32 *ZmEA1* cDNA clones were identified, which suggests a high level of expression in mature egg cells. Further studies showed that *ZmEA1* is an intronless single gene in maize but may represent a member of a relatively heterologous gene family based on weak genomic Southern hybridization signals. Homologous sequences are also present as single genes in barley, pearl millet, and *Tripsacum dactyloides*. Interestingly, two closely physically linked (4-kb) homologs appear to be present in rice [*Oryza sativa EA-like* 1 (*OsEAL1*), BAC83883.1, and *OsEAL2*, BAC83885.1 (Fig. 1A)], as shown by genomic Southern and database analyses. No obvious homologs were identified in *Arabidopsis thaliana* or other dicotyledonous plant species, which suggests a possible Gramineae specific conservation of *EA1*-like genes.

The *ZmEA1* promoter (*ZmEA1*p) was isolated as 1570 base pairs of genomic sequence 5′ of the AUG initiation codon and used for transgenic analyses of promoter and protein functions in the deeply embedded female gametophyte of maize (Fig. 2A). The promoter was fused to the β-glucuronidase (*Gus*) reporter gene. GUS activity in three of four independent functional *ZmEA1*p*::GUS* transgenic lines was exclusively detected in the egg apparatus of unpollinated mature ovules, confirming the egg apparatus specificity of the *ZmEA1*p transcriptional regulation (Fig. 2D). Unfertilized ovules from a transgenic maize line expressing GUS under control of a rice actin promoter (*OsACT*p:: *GUS*) were used to show that staining in all cells of the female gametophyte could be detected (Fig. 2E). A ZmEA1:GFP C-terminal fusion protein regulated by the *ZmEA1*p was secreted from the egg apparatus to the micropylar region of the nucellus of four independent transgenic lines in a manner dependent on floral developmental stage. After silk emergence, the ZmEA1:GFP first accumulated in the filiform apparatus (egg apparatus cell walls) (Fig. 3, A and B). After silk elongation (>10 cm), GFP signal was extended to a restricted area of the nucellus of unfertilized ovules (Fig. 3, C to F). The increase of GFP signal was well correlated with maturation of the egg apparatus during the female receptive period (*9*). Confocal laser scanning microscopy (CLSM) observations confirmed the presence of cell wall–localized GFP signals spreading from the egg apparatus toward the surface of the nucellus at the micropylar opening of the ovule (Fig. 3, E and F). This suggests possible proteolysis of the conserved C-terminal region from the predicted ZmEA1 transmembrane domain to allow secretion and transport of

[1]Biocenter Klein Flottbek, Developmental Biology and Biotechnology, University of Hamburg, Ohnhorststrasse 18, D-22609 Hamburg, Germany. [2]Bayer BioScience N.V., Technologiepark 38, B-9052 Ghent, Belgium.

*To whom correspondence should be addressed. E-mail: dresselh@botanik.uni-hamburg.de